Review Paper

Comparison of average crystallite size by X-ray peak broadening and Williamson–Hall and size–strain plots for VO^{2+} doped ZnS/CdS composite nanopowder

J. Madhavi[1]

Received: 5 July 2019 / Accepted: 16 September 2019 / Published online: 29 October 2019

Abstract
The paper deals with the exhaustive study and analysis of VO^{2+} ions doped ZnS/CdS composite nanopowder with the help of X-ray peak profile analysis (XPPA). The investigation has been carried out by applying a distinct pattern of Williamson–Hall (W–H) approach viz., uniform deformation model, the uniform stress deformation model and uniform deformation energy density model, and size strain plot (SSP). Fourier transforms infrared spectroscopy (FT-IR), scanning electron microscope and energy dispersive spectra (EDS) and transmission electron microscope (TEM) techniques. The XRD study is high manipulated order and fundamental focus is on phase identification, with some analysis on advanced concepts such as crystallite size and lattice strain have been estimated using the modified form of the W–H methods. XRD pattern confirmed that the structure of the sample belongs to the cubic system. The variation of lattice constant (a) with dopant is assigned to Vegard's law. The root means square strain was identified from the interionic separation and lattice strain assumed on W–H models. FT-IR spectrum exhibited characteristic vibrational modes of Zn and Cd ions along with other bands. EDS analysis gives information about the elemental composition in the present sample. The shape of VO^{2+} ions doped ZnS/CdS composite nanopowder was spherical in TEM images. The result showed that there was a good agreement in the particle size obtained from the W–H method and the SSP method with TEM images.

Keywords X-ray diffraction · FT-IR · Co-precipitation method · W–H plots

1 Introduction

The mechanical behavior of micro/nanoscale substance differs for their properties in terms of bulk nature, and it is familiar that "Small or nano range particles are stronger when compare to bulk materials in the present research". Until now, electron microscopy is being used to analyze the small-scale techniques of objects placed on in situ and ex situ classification. The limitation of electron microscopy technique is a two-dimensional design of top surface from thin-sheet like foil of matter. Over the past twenty years, a large advancement is attained at third group synchrotrons that hard X-ray beam can target lowering down to the 100-nm size [1]. A synchrotron is a certain class of regular particle accelerator, which can transfer the energy of the high-speed electrons into a strong-energy poly-chromatic X-ray beam [2]. The strength of this mechanism as internal stress, research investigation for micro- and the nanoscale instrument is the estimation of stresses along with sub-micron clarity, the assessment of the unequal principal-stresses, and the evaluation of hydrostatic elements of the stress tensors [3]. Synchrotron diffraction contained three types of techniques namely X-ray scattering, pair distribution function (PDF), X-ray diffraction (XRD) and X-ray absorption spectroscopy (XAS) [4] which can substantially provide structural characteristics of materials with

✉ J. Madhavi, madhavij03@gmail.com | [1]Department of Physics, University College of Sciences, Acharya Nagarjuna University, Nagarjuna Nagar, Guntur 522510, India.

SN Applied Sciences (2019) 1:1509 | https://doi.org/10.1007/s42452-019-1291-9

a greater conclusion and completely 3D [1]. During current research dimensions of physics, chemistry, and fabric science, transition metal oxides with nanostructure had mesmerized considerable absorption for the last couple of years concentrate of they are modern electrical and optical address with semiconductor crystals with massive binding energy (60 meV) [5]. Currently, emergent attention has been given to composite nanoparticles taking into consideration that the association of two semiconductor nanocrystals will foremost to a sequence of novel optical and digital residences [6, 7]. Nanostructured semiconductors of type II-VI which are observed to be the leading substance because they are an advantage in a lot of fields like fuel, sensors [8], photoconductors, imaging, solar cells, biological detection, UV sensors, quick wavelength laser diodes, and different luminescence instruments [9, 10]. Amongst II-VI compound semiconductors nanosize particles, Zinc, and cadmium sulfide are mostly useful for the majority part of the promising materials for greater results [11]. Zinc sulfide is a well-ordered nanoscale semiconductor compound for detecting UV [12], visible light considering that of its foremost energy gap of 3.68 eV (345 nm) and extreme reactivity. It has a wide range of possible applications in optoelectronics, optics, and solar energy devices [13, 14]. Cadmium sulfide with a direct bandgap of 2.42 eV (515 nm) [15] has a purpose in window layer materials, [16] LEDs [17] and photodetectors [18]. Its purposes in photodetectors and solar cells when used at the part of in conjunction with narrow energy gap components like CdTe CdSe, CdO etc., in a similar way the nanocomposite matching of band gaps between any two add-ones of II-VI Semiconductor NCs, for illustration of CdSe/ZnS [19] CdS/ZnS [20], CdSe/CdS [21] and ZnO/ZnS [22] has been drastically concerned for the development of the charge transfer efficiency. The doping with transition metal ion VO^{2+} ions brought a tremendous alteration in structural properties. Additionally, to the easier properties, VO^{2+} ions doped ZnS/CdS composite nanopowder illustrates reveals further promising functions in the subject of sensors, optoelectronics [23], and ferroelectric memory devices. Doped ZnS/CdS composite nanopowder particles were incorporate with the assistant of remarkable physical and chemical procedure such as spray pyrolysis, RF sputtering, electrochemical deposition, chemical vapor deposition, chemical precipitation and, sol–gel methods [24–31]. Among all these methods, chemical precipitation was more appropriate and suitable procedure due to simplicity, energy-efficient and eco-friendly route to produce VO^{2+} ions doped ZnS/CdS composite nanopowder [32]. Secondly, comparative reviews of the suggest particle dimension from the powdered XRD, W–H models, FT-IR, SEM, EDS and TEM measurements. As the study of analytical quantity of dislocation densities are an extremely great deal with TEM investigation. The study of dislocation bend in irradiated substances is also constrained using TEM analysis [33]. The concept of Diffraction peak profile investigation is a highly useful technique to explore the dislocation density, dislocation structure, and population distribution in the technically deformed objects due to such a reason which is a foundation to be a complementary procedure to TEM analysis [34, 35].

At present, XRD was employed in three types of diffraction techniques containing, powder diffraction, single-crystal XRD, and grazing incidence angle diffraction. A black and white X-ray beam of light is used in these experiments [36]. XRD pattern is an acceptable approach to estimate the structural and phase characteristics of single crystals and/or polycrystalline components. Investigation of the mechanical action of micro-/nano size, structures of the electronic device highly essential. Crystallite size has an excellent coherent diffraction domain in XRD. Moreover, the average crystallite size of the particles varied as to the particle size as a result of the existence of grain boundaries and/or polycrystalline aggregates [37]. The formation of strain in the crystalline lattices may be created by various reasons for example lattice dislocations, crystal imperfections, triple junctions, grain boundary, sinter or contract stresses, Coherency stresses stacking faults, etc., [38]. Based on the present XRD pattern, several approaches have been employed to determine the lattice strain and crystallite dimension of elements. Under such a research scenario, we implement three models including Scherrer's, W–H models and size–strain plot (SSP) methods. In Scherrer's method, the crystallite size was measured using the maximum intensity of the diffraction peak in the present X-ray diffraction pattern. The Bragg width involvement produced based on crystallite size is in inverse relation to the crystallite size. Although, it should be noted that, the influence of non-uniform strain and instrumental results on the peak broadening has not been mentioned in Scherrer's method. Thus, Scherrer's method suggested only a lesser limitation on the average crystallite size [39]. Along with several ways to study and/or evaluate the mean crystallite size and lattice strain attention to the peak profile analysis [Warren–Averbach (W–A) method, Fourier technique, W–H models, and Rietveld refinement technique], W–H analysis is a convenient procedure to estimate the average crystallite size and lattice strain-induced peak broadening taken account into consideration the shift in peak broadening against with an deflection angle of position 2Theta.

During the current research analysis on VO^{2+} ions doped ZnS/CdS composite nanopowder was synthesized through co-precipitation method. It has been found that this procedure is a simple method and rapid, gentle, energy-efficient and eco-friendly route to develop VO^{2+}

ions doped ZnS/CdS composite nanopowder. Secondly, comparable evaluations of the essential element dimension, precise information about a small volume of sample can discern crystallite shape, as well as size and weight and atomic weight percentage in the prepared sample, can be found from TEM and SEM–EDS analysis. Subsequently, the effect of single concentration (0.01 mol%) of vanadium dopant was investigated on the morphological study of ZnS/CdS composite nanopowder. Transition metal (TM) at a small concentration does not seem to produce noticeable distortions in the structure [40]. The unit cell parameters slightly change with dopant content which shows effectively built into the host lattice due to this there is no secondary diffraction peaks from other crystalline forms are noticed [41]. In the present study, the crystallite size of VO^{2+} ions doped ZnS/CdS composite nanopowder gives the structural parameters such as average particle size (**D**), microstrain (**ε**) and dislocation density (**δ**) values are evaluated from Scherrer's method and W–H Analysis. The average crystallite size from XRD is highly correlated with TEM analysis. In extension, the lattice strain was approximated with three W–H models, specifically, (UDM), (USDM), (UDEDM), and (SSP). This analysis outperforms the study which has been made so far.

2 Experimental

2.1 Materials

All chemical reagents which are of the analytical grade, and have been purchased from pure Merck chemical supplies, India. The new synthesized route of a VO^{2+} ion-doped ZnS/CdS composite nanopowder were used in particular Zinc acetate $Zn(CH_3COO)_2$, Cadmium acetate $Cd(CH_3COO)_2$, Sodium sulfide (Na_2S), Vanadium pentoxide (V_2O_5) and Ethanol were used as sources. Deionized water was used for all dilution and sample preparation. All the chemicals are above are 99% purity. All the glass wear used in this experimental was acid washed.

2.2 Preparation of VO^{2+} ions doped ZnS/CdS composite nanopowder

VO^{2+} ions doped ZnS/CdS composite nanopowder was successfully synthesized by co-precipitation method at room temperature. The powder form of a zinc acetate 0.2 mol% was dissolved in 50 mL same amount of water–ethanol matrix to an equal molar amount of Na_2S aqueous solution were mixed drop by drop. The collection of sample mixture was stirred magnetically at 80 °C until a homogeneous milky white precipitate formed. This is the indication of the formation of ZnS nanoparticles. For the next step, 0.09 mol% of cadmium acetate powder was dissolved in a 50 mL equal volume of the water–ethanol matrix which is added to the above colloidal solution then stirred steadily. After 10 min, 0.1 mol% of Na_2S 50 mL (prepared in a deionized water–ethanol matrix) solution was mixed dropwise in the above solution, subsequently, after 4 h of continuous stirring, the milky white solution turned to pale yellow colored voluminous precipitate appeared which indicates the composition of ZnS/CdS nanoparticles. Lastly, 0.01 mol% of V_2O_5 dissolved in 50 mL identical volumes of water–ethanol matrix added to the above composite solution and stirred constantly for 3 h. The obtained solution was washed several times with deionized water to remove undesirable impurities. Then the solution was kept in an ultracentrifuged at 10,000 rpm for about 30 min. The fine powder was collected and dried in a hot air oven at 120 °C for 2 h and grind with agate motor by hand milling. Finally synthesized VO^{2+} ions doped ZnS/CdS composite nanopowder was obtained and characterized by different techniques.

2.3 Characterization

Powder X-ray diffraction pattern (XRD) of the prepared sample is recorded on Shimadzu XRD 6100 diffractometer. Fourier Transformed Infrared (FT-IR) spectrum was recorded by using KBr pellet on Shimadzu IR Affinity-Is in the range 4000–400 cm^{-1}. Scanning Electron Microscope (SEM) and Energy Dispersive X-ray Spectroscopy (EDS) images were taken from ZEISS EVO 18. Transmission electron microscope (TEM) images are recorded on HITACHI H-7600 and CCD CAMERA system AMTV600 by dispersing the samples in ethanol.

3 Results and discussion

3.1 Structural properties

The X-ray diffraction pattern of the prepared VO^{2+} ions doped ZnS/CdS composite nanopowder was depicted in Fig. 1 all exhibited XRD peaks were listed by using ZnS and CdS structure with cubic phase, well-matched with (JCPDS) card for ZnS is (05-0566) and for CdS is (80-0019) respectively. The prepared composite nanopowder exhibits an intense as well as narrow width sharp peaks enables the good crystallinity [42]. The peak position shift with transition metal ion doping reveals the changes in the lattice parameters. The lattice constants for cubic structure (a = b = c), the cell volume obtained from the XRD pattern [43]. Apart from the X-ray peak profile evaluation (XPPA) mentioned that a very fine composite nanopowder of ZnS and CdS peaks are present in

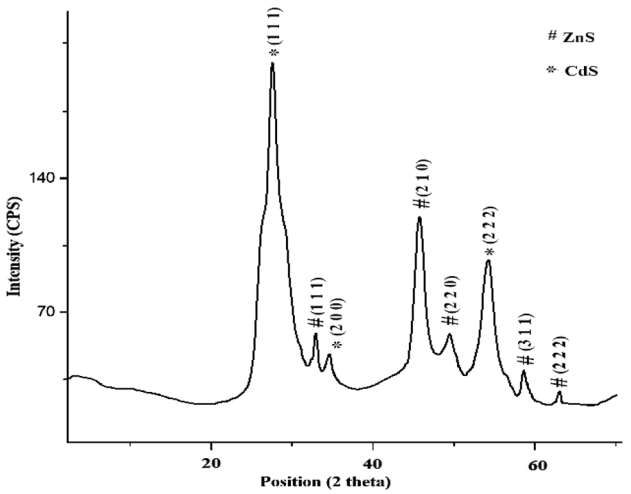

Fig. 1 XRD pattern of VO^{2+} ions doped ZnS/CdS composite nanopowder

the sample. There are no observable characteristic peaks of VO^{2+} ions are noticed in the present X-ray diffraction; due to this, some distortion will be created in the structure of the host lattice. The broadening within the height naturally confirms the XRD outcome that tiny nanoparticles are reflected in the pattern. From Bragg's diffraction,

$$2\mathbf{d}\sin\theta = \mathbf{n}\lambda \tag{1}$$

where 'θ' is the glancing angle, n is an integer which suggests the order of diffraction more often than not than no longer (n = 1), λ (= 1.5406 Å) is the wavelength of X-rays. The interatomic distance (d) is interrelated to the lattice constant parameter "**a**" and the lattice parameters <h k l> for cubic formation through the following relation [44]

$$\mathbf{d} = \frac{\boldsymbol{a}}{\sqrt{\boldsymbol{h}^2 + \boldsymbol{k}^2 + \boldsymbol{l}^2}} \tag{2}$$

For the Estimation of the first order, n = 1;

$$\sin^2\theta = \frac{\lambda^2}{4}\frac{[h^2 + k^2 + l^2]}{a^2} \tag{3}$$

The lattice constant as **a** for simple cubic ZnS and CdS planes are <1 1 1> and <1 1 1> computed by the relation

$$\mathbf{a} = \left(\sqrt{3}\lambda\right)/(2\sin\theta) \tag{4}$$

The lattice constant as ***a*** for the simple cubic ZnS is 5.4144 Å and CdS is 5.7726 Å corresponding unit cell volumes for simple cubic: ZnS = 158.72 cm^3 and cubic CdS = 192.36 cm^3. The diffraction peaks corresponding to the planes <1 1 1>, <2 0 0>, <2 2 0>, <3 1 1> and <2 2 2> are consistent with XRD data of ZnS and <1 1 1>, <2 0 0> and <2 2 2> for CdS. Comparison of (d_{hkl}), percentage of variation of d and FWHM from XRD, JCPDS card and corresponding <*h k l*> planes, are shown in Table 1.

Table 1 Interplanar spacing (d_{hkl}) from XRD, JCPDS data card for corresponding <*h k l*> planes, percentage of variation of d, and FWHM for VO^{2+} ions doped ZnS/CdS composite nanopowder

<h k l>	d_{XRD} (Å)	d_{JCPDS} (Å)	% of contraction in d	FWHM (°)
<1 1 1>	3.3329	3.2321	0.0021	0.7872
<1 1 1>	3.1261	3.0574	0.0224	0.3936
<2 0 0>	2.8863	2.8200	0.0224	0.4723
<2 0 0>	2.7072	2.5931	0.0439	0.4723
<2 2 0>	1.9145	1.9709	0.0285	0.3936
<2 2 2>	1.6664	1.6907	0.0180	1.1021
<3 1 1>	1.6325	1.6219	0.0065	0.0900
<2 2 2>	1.5630	1.5737	0.0026	0.5760

3.2 Debye–Scherer's procedure

The width of the peak broadening evidence grain refinement at the side of the significant stress associated with the energy. Fixed material such as silicon is used to verify the significant broadening. The instrumental corrected enlargement (β_{hkl}) [45] comparable to every diffraction peak of VO^{2+} ions doped ZnS/CdS composite nanopowder making use of the relation as follows [46]

$$\boldsymbol{\beta_{hkl}} = \mathbf{b}\,[(\boldsymbol{\beta}^2_{\mathbf{hkl}})\text{Measured} - (\boldsymbol{\beta}^2_{\mathbf{hkl}})\text{Instrumental}]^{1/2} \tag{5}$$

For a precise size and strain, the configurational analysis and crystallite size and identification of phase of composition sample were performed by the peak broadening as shown in Fig. 1 the evaluated grain size from the XRD peak by using the Scherer's formula [47] is given by the following Eq. (6)

$$\mathbf{D_{sch}} = \mathbf{k}\lambda/\boldsymbol{\beta}_{\mathbf{hkl}}\cos\theta \tag{6}$$

For spherical shape k is equal to 0.98, β_{hkl} is the essential half-width, λ is the wavelength of Cu-kα radiation of the incident X-ray (λ = 0.15406 nm), D is the average particle size which is in the order of nanoscale and θ is peak positions for corresponding <h k l>. For VO^{2+} ions doped ZnS/CdS composite nanopowder, the calculated value of the crystallite dimension is (D) 10.39 nm. Additionally, the dislocation density δ used to be calculated using Williamson and Small man's formula in lines/m^2 [48]

$$\boldsymbol{\delta} = \mathbf{n}/\mathbf{D}^2 \tag{7}$$

where n is approximately equal to 1 [49]. The dislocation density (δ) is 9.2462×10^{15}lines/m^2. This microstrain arises from the large fraction of exterior atoms and unsaturated affecting bonds, which may be responsible for really a lot of unique chemical and physical properties of the nanoparticles. The strain influence broadening appeared from crystal irregularity and distortion can be related in Eq. (8).

$$\boldsymbol{\beta}_{\varepsilon} = \mathbf{C}\varepsilon\tan\theta \tag{8}$$

$$\varepsilon = \beta_{hkl}/4\tan\theta \tag{9}$$

3.3 Approximation of microstrain (ε)

3.3.1 Williamson–Hall (W–H) models

W–H system [50] is dependent upon the principle which gives the knowledge about size broadening and stress broadening (βε) concerning Bragg viewpoint (θ) extent enlarge will also be interconnected to Debye-Scherer's (β_{DS}) method as in Eq. (6). The strain-induced broadening coming up from crystal irregularity and distortion may also be associated in Eq. (9).

$$B\varepsilon = C\varepsilon\tan\theta \tag{9.1}$$

the place, ε is examined from the determined broadening and C is the regular equivalent to 4 that is dependent upon the assumptions made involving the identity of the inhomogeneous stress [51].

3.4 Uniform deformation model (UDM)

As stated by W–H method, the enlargement of the coherent scattering neighborhood is found to be of finite and the internal stress in the arranged compound. In Williamson–Hall proposal the powder X-ay diffraction peak broadening confirms the particle dimension and strain internally. Peak profile evaluation through W–H models and SSP differentiates between strain and size broadening of the peak is considering a consequence of Bragg angle (**2θ**). The strain effect broadening in composite nanoparticles are approximate distortion and imperfections were estimated by the mechanism,

$$\varepsilon = \beta_{hkl}/4\tan\theta \tag{10}$$

The width of the peak confirms 1/cosθ varies with crystallite size and tan θ varies as strain, by adding these two present in the composite nanopowder and can be written as

$$\beta_{hkl} = \beta_D + \beta_\varepsilon \,(\text{or})\, \beta_{hkl} - \beta_\varepsilon = \beta_D \tag{11}$$

The location β_D suggests crystallite dimension contribution and βε prompted through making use of brought about stress broadening and β_{hkl} stated FWHM of instrumental broadening with corrected dimension. The X-ray powder diffraction of each peak is analyzed with the help of the instrumental broadening if the stress and particle dimension contribution are usually no longer based on each different and are independent of every extraordinary and have a Cauchy-equation [52].

From Eqs. (6) and (9)

$$\beta_{hkl} = k\lambda/D\cos\theta + 4\varepsilon\tan\theta \tag{12}$$

By way of rearranging Eq. (12), we get

$$4\varepsilon\sin\theta_{hkl} + k\lambda/D = \cos\theta_{hkl} \tag{13}$$

From the linear fit of the report a plot of $4\sin\theta_{hkl}$ versus $\beta\cos\theta_{hkl}$, as shown in Fig. 2a the average crystallite size and the microstrain (ε) were obtained from the y-intercept. Strain due to the result of reduction inside the lattice values is $\varepsilon = 3.333 \times 10^{-3}$, D = 11.51 nm as summarized in Table 2.

3.5 Uniform stress deformation model (USDM)

Inside entire crystallographic supervision, the deformation stress inside the lattice is uniform and a small microstrain is to be assumed inside the present grain. In order with Hooke's law stated as $\sigma = \varepsilon Y_{hkl}$ where σ is the stress of the lattice, ε is anisotropic micro stress and Y_{hkl} is the modulus of elasticity. This equation is equitable for small stress. When pressure is extended the particles depart from this correspondence. In this attainment the W–H equation [25] is reshaping through utilizing incorporating (ε) in Eq. (13) we get

$$K\lambda/D + 4\sigma\sin\theta_{hkl}/Y_{hkl} = \beta_{hkl}\cos\theta_{hkl} \tag{14}$$

For cubic crystal, Y_{hkl} is given by [26]

$$Y_{hkl} = \left(\frac{\left(\left[h^2 + \frac{(h+2k)^2}{3} + \left(\frac{al}{c}\right)^2 \right]^2 \right)}{S_{11}\left(h^2 + \frac{(h+2k)^2}{3}\right)^2 + S_{33}\left(\frac{al}{c}\right)^4 + (2S_{13} + S_{44})\left(h^2 + \frac{(h+2k)^2}{3}\right)\left(\frac{al}{c}\right)^2} \right) \tag{15}$$

The place S_{11}, S_{33}, S_{13}, S_{44} are the elastic compliances for CdS are 2.069×10^{-11}, 1.594×10^{-11} (-0.497×10^{-11} m^2 N^{-1}), 6.412×10^{-11} m^2 N^{-1} and for ZnS are 1.108×10^{-11}, 0.86424×10^{-11}, (-0.2216×10^{-11} m^2 N^{-1}), 2.157×10^{-11} m^2 N^{-1} [53, 54] and a, b and c are lattice parameters of VO^{2+} doped ZnS/CdS nanoparticles respectively [55]. The calculated value of the total Young's modulus (Y_{hkl}) for VO^{2+} ions doped cubic ZnS and CdS composite nanopowder is approximately equal to 144.54×10^9 GPa which holds good with the theoretical values and is found to be 125.01×10^9 GPa. The plot is drawn between $\beta_{hkl}\cos\theta_{hkl}$ as a function of $4\sin\theta_{hkl}/Y_{hkl}$ Fig. 2b. The uniform deformation stress 'σ' can be calculated from the slope

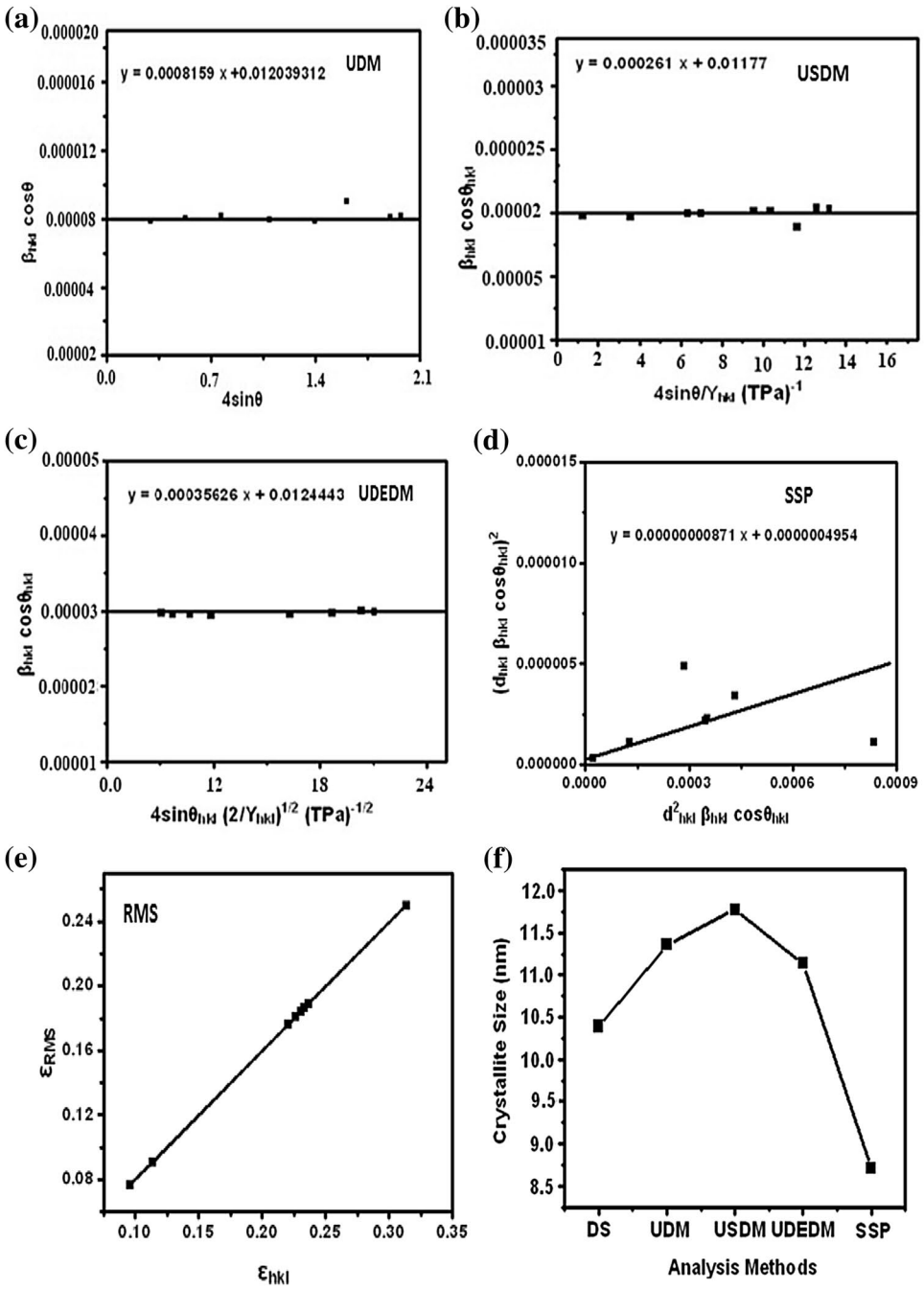

Fig. 2 **a** Plot of $\beta\cos\theta_{hkl}$ versus $4\sin\theta_{hkl}$ for VO^{2+} ions doped ZnS/CdS composite nanopowder. **b** Plot of $\beta_{hkl}\cos\theta_{hkl}$ versus $4\sin\theta_{hkl}/y_{hkl}$ for VO^{2+} ions doped ZnS/CdS composite nanopowder. **c** Plot of $\beta_{hkl}\cos\theta_{hkl}$ versus $4\sin\theta_{hkl}(2/y_{hkl})^{1/2}$ for VO^{2+} ions doped ZnS/CdS composite nanopowder. **d** Plot of $(d_{hkl}\beta_{hkl}\cos\theta_{hkl})^2$ versus $(d^2_{hkl}\beta_{hkl}\cos\theta_{hkl})$ for VO^{2+} ions doped ZnS/CdS composite nanopowder. **e** Plot of ε_{rms} versus ε_{hkl} for VO^{2+} ions doped ZnS/CdS composite nanopowder. **f** Comparison of Scherer's with W–H models for VO^{2+} ions doped ZnS/CdS composite nanopowder

of the linear fit and the crystallite dimension offers the y-intercept. If Y_{hkl} of ZnS/CdS composite nanopowder can also be acknowledged, stress-energy **ε** can be known and evaluated given in Table 2.

3.6 Uniform deformation energy density model (UDEDM)

When u_{ed} is strain-energy density and is a function of stress is $u_{ed} = (\varepsilon^2 Y_{hkl})/2$ for elastic nature of a technique adopted with the aid of Hooke's law, Eq. (14) will also be modified using [56].

$$\mathbf{B_{hkl}\cos\theta_{hkl}} = (\mathbf{k\lambda/D}) + (\mathbf{4\sin\theta_{hkl}}(\mathbf{2u_{ed}/Y_{hkl}})^{1/2} \quad (16)$$

The Plot of $\beta_{hkl}\cos\theta_{hkl}$ versus $(4\sin\theta_{hkl}\ (2/Y_{hkl})^{1/2})$ is depicted in Fig. 2c and slope of the linear fit information represents the value of u_{ed} and y-cut mentioned the average crystallite size (D). Where $u_{ed} = (\varepsilon^2 Y_{hkl})/2$ and linearity between stress and strain is given by $\sigma = \varepsilon Y_{hkl}$ where the σ

Table 2 Geometric parameters for synthesized VO^{2+} ions doped ZnS/CdS composite nanopowder

Scherrer method	Williamson–Hall method								Size–strain plot			
	UDM		USDM			UDEDM						
D (nm)	**D** (nm)	$\varepsilon \times 10^{-3}$	**D** (nm)	$\varepsilon \times 10^{-3}$	**σ** (MPa)	**D** (nm)	$\varepsilon \times 10^{-3}$	**σ** (MPa)	u_{ed} (kJ m^{-3})	D_V (nm)	ε		**σ** (MPa)
											$\varepsilon_a \times 10^{-3}$	$\varepsilon_{RMS} \times 10^{-4}$	
13.9	11.51	0.81	11.77	2.61	378	11.14	1.32	191	126	8.71	3.52	7.03	510

was calculated from $u_{ed} = (\sigma^2/2Y_{hkl})$. By knowing Y_{hkl} value, the lattice strain can even be calculated.

3.7 Size-strain plot (SSP)

The 'Gaussian feature well-known shows strain' and the "crystallite measurement" profile through Lorentzian function [57]. A different class of evaluation the dimensions stress plot specifications can also be obtained through SSP plot for anisotropic line broadening

$$\left(\mathbf{d_{hkl}\beta_{hkl}cos\theta_{hkl}}\right)^2 = \mathbf{1/v_{s.}}\left(\mathbf{d_{hkl}^2\beta_{hkl}cos\theta_{hkl}}\right) + \left(\varepsilon_a/2\right)^2 \tag{17}$$

where d_{hkl} is the inter-planar spacing, v_s is the volume-weighted acceptable size and ε_a is a evaluate of the apparent stress which is related to root-mean stress (RMS)

$$\langle \varepsilon_{rms} \rangle = \left(\varepsilon_a\right)/2\sqrt{2\pi} \tag{18}$$

the volume-weighted actual dimension for spherical crystallites is given with the aid of

$$\mathbf{Dv = Vs(4/3)} \tag{19}$$

The corresponding slope for VO^{2+} ions doped ZnS/CdS composite nanopowder have been bought from a plot of $\left(d_{hkl}\beta_{hkl}\cos\theta_{hkl}\right)^2$ versus $\left(d_{hkl}^2\beta_{hkl}\cos\theta_{hkl}\right)$ as shown in Fig. 2d. For all diffraction peaks of VO^{2+} ions doped ZnS/CdS composite nanopowder with the cubic single-phase deflections from $2\theta = (0°–70°)$. The particle size D_V is calculated from the slope of the fitted data and the cut off from RMS value was neglected. According to the literature report, isotropic is due to line broadening and the least-squares lines through the points had a non-zero intercept and a positive slope [58]. Comparison of SSP, William, and Hall the lattice strain (ε) is in the first-rate contract with every other in Table 2. Conversely, the SSP procedure is appropriate in evaluation with W–H models for the reason that much less value is given to potential from reflections at excessive angles and the points are linearly fitted. Comparing the entire primary three W–H models, UDM confirm the homogeneous isotropic identity of the crystal whereas USDM and UDEDM confirm the anisotropic nature. In USDM and UDEDM, it most often is noted that even though every Eqs. (14) and (15) are taken into consideration within the anisotropic character of the elastic regular, they are almost specified. Equation (16) reveals deformation energy u_{ed} to be homogeneous in all crystallographic in order.

From all methods, the estimated values from the y-cut of the graphs consistent with the conventional crystallite size are found to be 11.36, 11.77, 11.12 and 8.71 nm respectively as shown in Table 2. This is almost similar and also in the order of nanoscale. From the SSP approach, the

crystallite dimension value is in well-matched with Scherrer's method and is in evaluation with W–H models. From these studies, our values are more appropriate to the literature report [30]

3.8 Estimation of RMS strain

According to the Wilson method, the maximum value (ε_{hkl}) and root-mean-square micro strains (ε_{rms}) across crystallographic planes (h k l) are related by [31, 59].

$$\varepsilon_{hkl} = \left(\Delta d_{hkl}/d_{ohkl}\right) \tag{20}$$

$$\langle \varepsilon_{rms} \rangle = (2/\pi)^{1/2} \varepsilon_{hkl} \tag{21}$$

By the consideration of Gaussian microstrain distribution, RMS used to be derived from the maximum worth of the microstrain become derived from the Bragg's law by Wilson [26, 60].

Substituting ε_{hkl} value in the Eq. (21), the RMS value is given via the relation

$$\langle \varepsilon_{rms} \rangle = (2/\pi)1/2\left(\Delta d_{hkl}/d_{ohkl}\right) \tag{22}$$

where $\mathbf{d_0}$ and $\mathbf{d}$ represent the Observed, and calculated inter-planar distance values. Figure 2e plot of ε_{rms} versus ε_{hkl} is making an inclination of 45° to the x-axis, if the strain values hold good with the theoretical values then there is no discrepancy on the inter-planar spacing due to nature of the crystal [61]. The excess quantity of grain boundaries because of dislocations may just arise from the lattice stress in the VO^{2+} ions doped ZnS/CdS nanopowder particles.

The XRD peak broadening reveals crystallites size, microstrain, and instrumental broadening. In another way the cause of strain is interrelated to lattice irregularity, RMS strain gives the distortion value. The higher the value of RMS strain, the lesser is the crystallite size.

3.9 Structural parameter (texture coefficient)

The texture coefficient of each <h k l> plane is resolute from the X-ray diffraction pattern according to the following formula [62]

$$TC_{hkl} = \frac{\frac{I_{(hkl)}}{I_{0(hkl)}}}{\sum_N \frac{I_{(hkl)}}{I_{0(hkl)}}} \tag{23}$$

where I_{hkl} is the depth of (hkl) diffraction peak on the sample under examination; I_{ohkl} is the intensity of (hkl) plane on an arbitrary sample taken from a powder diffraction file (PDF) card, and N is the number of diffractions considered inside the chemical analysis.

It has unique conditions

1. If $TC_{(hkl)}$ (~ 1) for every <hkl> planes, then the nanoparticles are with a randomly oriented crystalline similar to the JCPDS card reference.
2. $TC_{(hkl)}$ (> 1) implies that the VO^{2+} ions doped ZnS/CdS nanoparticles include a larger degree of orientation alongside C-axis.
3. Zero < $TC_{(hkl)}$ < 1 point out the lack of grains aligned in that path. Finally, the average crystallite dimension and the strain values estimated from all W–H models reveals to very suitable and intimately to interrelated Fig. 2d–f.

4 FTIR study

FT-IR spectral analysis of VO^{2+} ions doped ZnS/CdS composite nanopowder show a few absorption peaks between 400 and 4000 cm^{-1} is shown in Fig. 3. The spectrum could be explained by the characteristic bands of ZnS and CdS peaks obtained by the samples and was achieved by stirring the solution during preparation. Spectral analysis showed a small peak at 449 cm^{-1} corresponds to (Cd-S) metal sulfur bond confirms the configuration of CdS [63, 64]. The bands observed at a frequency 521 and 614 cm^{-1} are ascribed to Zn–S bond and corresponding to zinc and sulfide stretching [65, 66] and strong absorption peak at 807 cm^{-1} is the combination of V–O stretching modes [67]. The band at 1105 cm^{-1} is attributed to C-O carboxylic acid. The bands at 1631 cm^{-1} are ascribed to the symmetric bending mode of H_2O molecule [68]. The peaks at 3433 cm^{-1} are assigned to the vibrational approach of O–H groups [69] as given by Table 3.

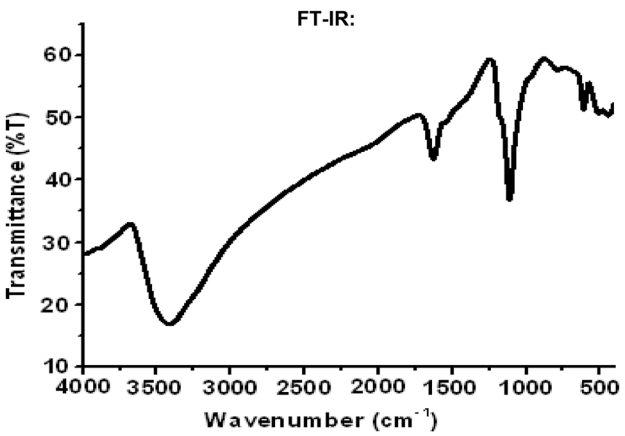

Fig. 3 FTIR spectra of Vo^{2+} ions doped ZnS/CdS composite nanopowder

Table 3 FTIR vibrational band assignments of VO^{2+} ions doped ZnS/CdS composite nanopowder

Vibrational frequency (cm^{-1})	Band assignments
449	Cd-S band
521, 614	ZnS
807	V–O stretching
1105	C–O carboxylic acid
1636	Symmetric bending vibration of H_2O
3433	–OH stretching

5 Morphological studies

The SEM images of VO^{2+} ions doped ZnS/CdS composite nanopowder are shown in Fig. 4. The micrograph shows with uniformly distributed with spherical like structure which in the size below 50 nm were observed. It also confirms that the particles are in the order of nanosize. The detailed microstructures of the product were further investigated using EDS and TEM techniques. The EDS analysis of the VO^{2+} ions doped ZnS/CdS composite nanopowder is as shown in Fig. 5. To verify the stoichiometric ratios from EDS analysis, the elemental composition from Zn to S is found to be ZnS and Cd to S is CdS the doping element VO^{2+} ratio and also reveal the atomic weight percentages of Zn = Cd = V respectively. Spectrum confirms the elemental composition (V, Zn, S, and Cd) of composite and the information of atoms on the surface tend to migrate to the subsurface layer [70]. TEM images of VO^{2+} ions doped ZnS/CdS composite nanopowder reveal that the structure of particles is in spherical as shown in Fig. 6. The average particle size of VO^{2+} ions doped ZnS/CdS composite nanopowder

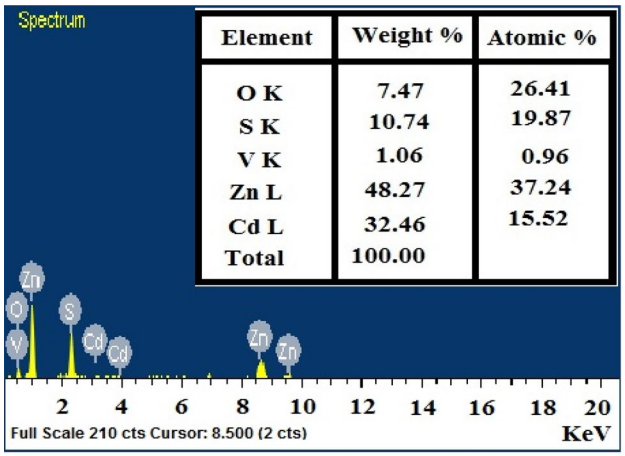

Fig. 5 EDX analysis Vo^{2+} ions doped ZnS/CdS composite nanopowder

is approximately 20 nm, which confirms the order of nanosize these results are well matched with XRD data and W–H models are inter-correlated with TEM analysis.

6 Conclusion

In this paper, VO^{2+} ions doped ZnS/CdS composite nanopowder was successfully synthesized by co-precipitation procedure and characterized by XRD, FT-IR, SEM–EDS and TEM analysis. Generally, XRD is adapted to support the evaluation of crystallites with a broad (or) multi-modal size distribution. From the X-ray peak broadening studies, it was noticed the intensity of the X-ray diffraction line depends on the elemental composition of the sample and its preparation conditions. The set of all values

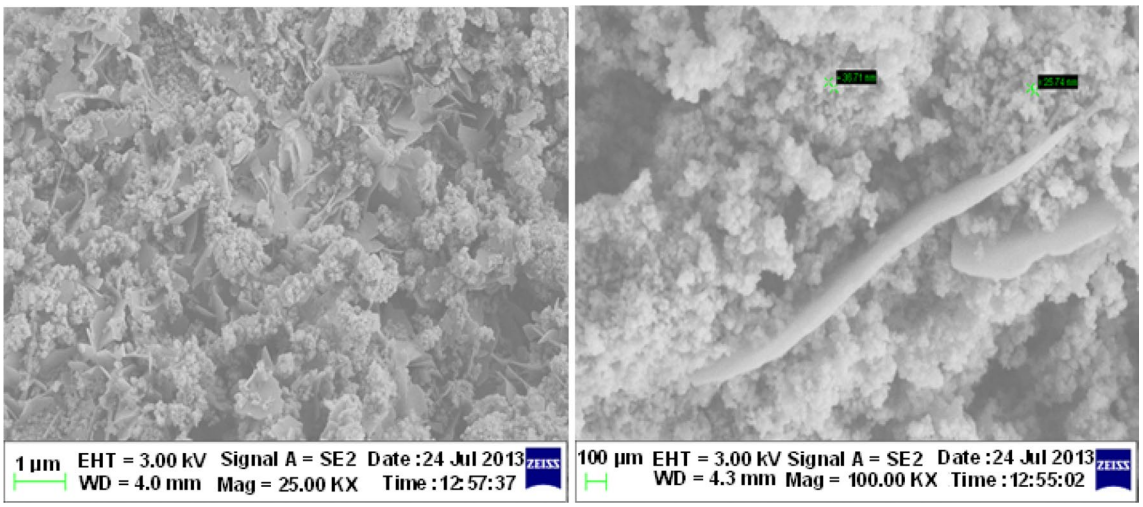

Fig. 4 SEM images of Vo^{2+} ions doped ZnS/CdS composite nanopowder

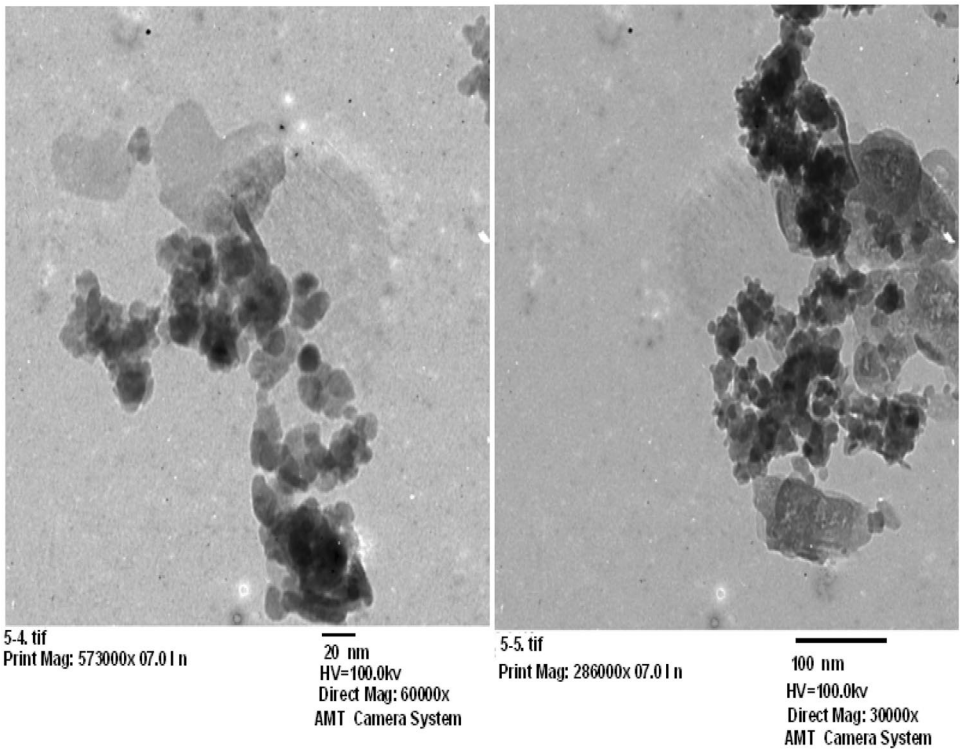

Fig. 6 TEM micrographs of Vo^{2+} doped ZnS/CdS composite nanopowder

of VO^{2+} ions doped ZnS/CdS composite nanopowder belong to the cubic structure. Observed X-ray diffraction peaks can be related to planes of atoms to assist in analyzing the atomic microstructure of a prepared sample. Both microstrain and crystallite size can be analyzed only when the broadening due to both are equivalent. The amount of microstrain is large the maximum observable crystallite size will be small. Due to vanadium ion doping causes the decrease in the crystallite size and enhanced the dislocation density, microstrain, and inter-planar spacing and also some lattice distortion will be created in the structure of the host material. Also, the estimated values of the mean particle size from the modified W–H plot and SSP methods are held a good agreement with TEM analysis.

Acknowledgements J. Madhavi would like to thank Acharya Nagarjuna University, Guntur for providing URF. Prof. RVSSN Ravi Kumar would like to thank the UGC-DSA1 and DST-FIST, New Delhi for providing financial assistance to the Department of Physics, Acharya Nagarjuna University to carry out the present research work.

Compliance with ethical standards

Conflict of interest The author(s) declare that they have no conflict of interests.

References

1. Cornelius TW, Thomas O (2018) Progress of in situ synchrotron X-ray diffraction studies on the mechanical behavior of materials aat small scales. Prog Mater Sci 94:384–434. https://doi.org/10.1016/j.pmatsci.2018.01.0042
2. Tippabhotla SK, Radchenkol I, Rengarajan KN, Illya G, Handara V, Kunz M, Tamura N, Budiman AS (2016) Synchrotron X-ray microdiffraction-probing stress state in encapusulated thin silicon solar cell. Procedia Eng 139:123–133. https://doi.org/10.1016/j.proeng.2015.09.2413
3. Budiman AS, Shin HAS, Kim BJ, Hwang SH, Son HY, Suh MS, Chung QH, Byun KY, Tamura N, Kunz M, Joo YC (2012) Measurement of stresses in Cu and Si around through-silicon via by synchrotron X-ray microdiffraction for 3-dimensional integratedcircuits. Microelectron Reliab 52:530–533. https://doi.org/10.1016/j.microrel.2011.10.016
4. Ferri D, Newton MA, Michiel MDI, Yoon S, Chiarello GL, Marchionni V, Matam SK, Aguirre MH, Weidenkaff A, Wen F (2013) Synctron highenergy X-ray methods coupled to phase sensitive analysis to characterize aging of solid catalyst with enhanced sensitivity. Phys Chem Chem Phys 15:8629–8639. https://doi.org/10.1039/C3CP44638G
5. Mak KF, Shan J (2016) Photonics and optoelectronics of 2D semiconductor transition metaldichalcogenides. Natphotonics 10:216226. https://doi.org/10.1038/nphoton.2015.28
6. Andrew N, Shioway E, Willner I (2000) Nanoparticle arrays on surfaces for electronic, optical, and sensor applications. Chem Phys Chem 1:18–52. https://doi.org/10.1002/1439-7641(20000804)

7. Rajeswar K, de Tacconi NR, Chenthamarakshan CR (2001) Semiconductor-based composite materials: preparation, properties, and performance. Chem Mater 13:2765–2782. https://doi.org/10.1021/cm010254z
8. Fang XS, Zhai TY, Gautam UK, Li L, Wu LM, Bando Y, Golberg D (2011) ZnS nanostructures: from synthesis to applications. Prog Mater Sci 56:175–287. https://doi.org/10.1016/j.pmatsci.2010.10.001
9. Sarmah S, Kumar A (2001) photo catalytic activity of polyaniline–TIO nano-composites. Indian J Phys 85:713–726
10. Mallick P, Rath C, Biswal P, Mishra NC (2009) Structural and magnetic properties of Fe doped NiO. Indian J Phys 83:517–523
11. Li Z, Yu LB (2019) The size effect of TiO_2 hollow microspheres on photovoltaic performance of ZnS/CdS quantum dots sensitized solar cell. Materials 12:1583. https://doi.org/10.3390/ma12101583
12. Soltani N, Saion E, Mahmood W, Yunus M, Navasery M, Bahmanrokh G, Erfani M, Reza Zare M, Gharibshahi E (2013) Photocatalytic degradation of methylene blue under visible light using PVP-capped ZnS and CdS nanoparticles. Sol Energy 97:147–154. https://doi.org/10.1016/j.solener.2013.08.023
13. Xu XJ, Hu LF, Gao N, Liu SX, Wageh S, Al-Ghamdi AA, Alshahrie A, Fang XS (2015) Controlled growth of ZnS nanoparticles to ZnS–CdS nanoparticles hybrids with enhanced photoactivity. Adv Funct Mater 25:445–454. https://doi.org/10.1002/adfm.201403065
14. Shin SW, Ra Kang S, Yun JH, Moholkar AV, Moon JH, Lee JY, Kim JH (2011) Effect of different annealing conditions on the properties of chemically deposited ZnS thin films on ITO coated glass substrates. Sol Energy Mater Sol Cells 95:856–863. https://doi.org/10.1016/j.solmat.2010.11.002
15. Goharshadi EK, Mehrkhah R, Nancarrow P (2013) Synthesis, characterization, and measurement of structural, optical, and phtotoluminescent properties of zinc sulfide quantum dots. Mater Sci Semicond Process 16:356–362. https://doi.org/10.1016/j.mssp.2012.09.012
16. Su B, Choy KL (2000) Microstructure and properties of the CdS thin films prepared by electrostatic spray assisted vapour deposition (ESAVD) method. Thin Solid Films 359:160–164
17. Kashiwaba Y, Sato J, Abe T (2003) Emission of lights of various colors from p-CdS:Cu/n-CdS thin-film diodes. Appl Surf Sci 212–213:162–165. https://doi.org/10.1016/S0169-4332(03)00058-8
18. Zhai T, Fang XS, Zeng H, Xu X, Bando Y, Golberg D (2010) Vapor-phase synthesis of one-dimensional ZnS, CdS, and $Zn_x Cd_{1-x}S$ nanostructures. Pure Appl Chem 82:2027–2053. https://doi.org/10.1351/PAC-CON-09-09-1
19. Talapin DV, Rogach AL, Haase M, Weller H (2001) Highly luminescent monodisperse CdSe and CdSe/ZnS nanocrystals synthesized in a hexadecylamine–trioctylphosphine oxide–trioctylphospine mixture. Nano Lett 1:207–211
20. Xie YP, Yu YuZB, Liu G, Ma XL, Cheng HM (2014) CdS–mesoporous ZnS coreshell particles for efficient and stable photocatalytic hydrogen evolution under visible light. Energy Environ Sci 7:1895–1901. https://doi.org/10.1039/c3ee43750g
21. Zhou J, Zhu M, Meng R, Qin H, Peng X (2017) Ideal CdSe/CdS core/shell nanocrystals enabled by entropic ligands and their core size-, shell thickness-, and ligand-dependent photoluminescence properties. J Am Chem Soc 139:16556–16567. https://doi.org/10.1021/jacs.7b07434
22. Yan J, Fang XS, Zhang L, Gautam UK, Sekiguchi T, Golberg D (2008) Structure and cathodo luminescence of individual ZnS/ZnO biaxial nanobelt heterostructures. Nano Lett 8:2794–2799. https://doi.org/10.1021/nl801353c
23. Wang Z, Zhang H, Zhang L, Yuan J, Yan SC, Wang C (2003) Low-temperature synthesis of ZnO nanoparticles by solidstate pyrolytic reaction. Nanotechnology 14:11–15
24. Erwin SC, Zu L, Haftel MI, Efros AL, Kennedy TA, Norris DJ (2005) Doping semiconductor nanocrystals. Nature 436:91–94
25. Kafashan H (2018) Comparison the effects of Se and Te inclusion on the physical and electrochemical properties of SnS thin films. Mater Sci Semicond Process 88:148–160. https://doi.org/10.1016/jmssm.2018.07.038
26. Xu XJ, Li SY, Chen JX, Cai S, Long ZH, Fang XS (2018) Design principles and material engineering of ZnS for optoelectronic devices and catalysis. Adv Funct Mater 28:1802029. https://doi.org/10.1002/adfm.201802029
27. Vijayalakshmi S, Venkatara JS, Jayavel R (2008) Characterization of cadmium doped zinc oxide (Cd:ZnO) thin films prepared by spray pyrolysis method. J Phys D Appl Phys 41:245403. https://doi.org/10.1088/0022-3727/41/24/245403
28. Najim JA, Rozaiq JM (2013) Effect Cd doping on the structural and optical properties of ZnO thin films. Int Lett Chem Phys Astron 15:137–150
29. Zargar RA, Khan SU, Khan MS, Arora M, Hafiz AK (2014) Synthesis and characterization of screen printed $Zn_{0.97}Cu_{0.03}O$ thick film for semiconductor device applications. Phys Res Int. https://doi.org/10.1155/2014/464809
30. Zargar RA, Santosh C, Shahabuddin MD, Kumar J, Arora M, Hafiz AK (2015) Novel composites of $Zn_{1-x}Cd_xO$ ($x=0$, 0.05, 0.1) thick films for optoelectronic device application. J Mater Sci Mater Electron 26:10027–10033. https://doi.org/10.1007/s10854-015-3683-y
31. Salavati-Niasari M, Soofivand F, Sobhani-Nasab A, Shakouri-Arani M, Hamadanian M, Bagheri S (2017) Facile synthesis and characterization of $CdTiO_3$ nanoparticles by Pechini sol–gel method. J Mater Sci Mater Electron 28:14965–14973. https://doi.org/10.1007/s10854-017-7369-5
32. Wu JCS, Chen CH (2004) A visible-light vanadium-doped titania nanocatalyst by sol–gel method. J Photochem Photobiol A 163:509–515. https://doi.org/10.1016/j.jphotochem.2004.02.007
33. Seymour T, Frankel P, Balogh L, Ungar T, Thompson SP, Jademas D, Romero J, Hallstadius L, Daymond MR, Ribarik G, Preuss M (2017) Evolution of dislocation structure in neutron irradiated Zircaloy-2 studied by synchrotron X-ray diffraction peak profile analysis. Acta Mater 126:102–113. https://doi.org/10.1016/j.actamat.2016.12.031
34. Ungar T, Gubicza J, Ribarik G, Borbely A (2001) Crystallite size distribution anddislocation structure determined by diffraction profile analysis: principle and practical application do cubic hexagonal crystals. J Appl Crystallogr 34:298–310
35. Chen X, Dejoie C, Jiang T, Ku CS, Tamura N (2016) Quantitative microstructural imaging by scanning laue X-ray micro- and nanodiffraction. MRS Bull 41:445–466. https://doi.org/10.1557/mrs.2016.97
36. Kumar H, Kumari A, Singh RR (2017) Tunable narrow emission in ZnS/CdS/ZnS quantum well structures prepared by aqueous route. Opt Mater 69:23–29. https://doi.org/10.1016/j.optmat.2017.04.009
37. Dinesha ML, Prasanna GD, Naveen CS, Jayanna HS (2013) Structural and dielectric properties of Fe doped ZnO nanoparticles. Indian J Phys 87:147–153. https://doi.org/10.1007/s12648-012-0182-3
38. Zhang JM, Zhang Y, Xu KW, Ji V (2006) General compliance transformation relation and applications for anisotropic hexagonal metals. Solid State Commun 139:87–91. https://doi.org/10.1016/j.ssc.2006.05.026
39. Sivakami R, Dhanuskodi S, Karvembu R (2016) Estimation of lattice strain in nanocrystalline RuO_2 by Williamson–Hall and size–strain plot methods. Spectrochim Acta A 152:43–50. https://doi.org/10.1016/j.saa.2015.07.008

40. Ahmed SA (2017) Room-temperature ferromagnetism in Co-, Cr-, and V-doped ZnO diluted magnetic semiconductor. Appl Phys A 123:440–448. https://doi.org/10.1007/s00339-017-1058-3
41. Saeki H, Thabata H, Kawai T (2001) Magnetic and electric properties of vanadium doped ZnO nanofilms. Solid Sate Commun 120:439–443
42. Krithiga R, Chandrasekaran G (2009) Synthesis, structural and optical properties of vanadium doped zinc oxide nanograins. J Cryst Growth 311:46104614. https://doi.org/10.1016/j.jcrysgro.2009.08.033
43. Hoa TT, Vu L, Canh T, Long NN (2009) Preparation of ZnS nanoparticles by hydrothermal method. J Phys Condens Matter 187:012081–012086. https://doi.org/10.1088/1742-6596/187/1/012081
44. Thandavan TMK, Gani SMA, San Wong C, Nor RM (2015) Evaluation of Williamson–Hall strain and stress distribution in ZnO nanowires prepared using aliphatic alcohol. J Nondestruct Eval 34:14–22. https://doi.org/10.1007/s10921-015-0286-8
45. Biju V, Neena S, Vrinda V, Salini SL (2008) 2008 Estimation of lattice strain in nanocrystalline silver from X-raydiffraction line broadening. J Mater Sci 43:1175–1179. https://doi.org/10.1007/s10853-007-2300-8
46. Sharma SureshKumarPankaj, Sharma Vineet (2012) CdS nanofilms: synthesis and the role of annealing on structural and optical properties. J Appl Phys 111:043519–043525. https://doi.org/10.1063/1.3688042
47. Liu H, Hu LF, Watanabe K, Hu XH, Dierre B, Kim BS, Sekiguchi T, Fang XS (2013) Cathodoluminescence modulation of ZnS nanostructures by morphology, doping, and temperature. Adv Funct Mater 23:3701–3709. https://doi.org/10.1002/adfm.201203711
48. Velumani S, Narayandass SaK, Mangalaraj D (1998) Structural characterization of hot wall deposited cadmium selenide thin films. Semicond Sci Technol 13(1016–10):24
49. Ghosh A, Kumari N, Tewari S, Bhattacharjee A (2013) Structural and optical properties of pure and Al doped ZnO nanocrystals. Indian J Phys 87:1099–1104. https://doi.org/10.1007/s12648-013-0346-9
50. Yadav Harsh, Sinha Nidhi, Goel Sahil, Kumar Binay (2016) Eu-doped ZnO nanoparticles for dielectric, ferroelectric and piezoelectric applications. J Alloys Compd 689:333–341. https://doi.org/10.1016/j.jallcom.2016.07.32
51. Pandiyarajan T, Karthikeyan B (2012) Cr doping induced structural, phonon and excitonic properties of ZnO nanoparticles. J Nanopart Res 14:647–656
52. Han SC, Hu LF, Gao N (2014) Efficient self-assembly synthesis uniform CdS spherical nanoparticles-Au nanoparticles hybrids with enhanced photoactivity. Adv Funct Mater 24:3725–3733. https://doi.org/10.1002/adfm.201400012
53. Zhang J, Zhang Y, Xu KW, Ji V (2016) General compliance transformation relation and applications for anisotropic hexagonal metals. Solid State Commun 139:87–91. https://doi.org/10.1007/s11051-011-0647-x
54. Ferahtia S, Saib S, Bouarissa N, Benyettou S (2014) Structural parameters, elastic properties and piezoelectric constants of wurtzite ZnS and ZnSe under pressure. Superlattice Microstruct 67:88–96. https://doi.org/10.1016/j.spmi.2013.12.021
55. Gaith M, Alhayek I (2009) Correlation between overall elastic stiffness, bulk modulus and interatomic distance in anisotropic materials: semiconductors. Rev Adv Mater Sci 21:183–191
56. Hazarika A, Peretz E, Dikovsky V, Santra PK, Shnek RZ, Sarma DD, Manassen Y (2014) STM verification of the reduction of the Young's modulus of CdS nanoparticles at smaller sizes. J Surf Sci 630:89–95. https://doi.org/10.1016/j.susc.2014.07.006
57. Gilbert B, Zhang H, Chen B, Kunz M, Huang F, Banfield JF (2006) Compressibility of zinc sulfide nanoparticles. J Phys Rev B 74:1154057. https://doi.org/10.1103/PhysRevB.74.115405
58. Tagliente MA, Massaro M (2008) Strain-driven (0 0 2) preferred orientation of ZnO nanoparticles in ion-implanted silica. Nucl Instrum Methods B 266:1055–1061. https://doi.org/10.1016/j.nimb.2008.02.036
59. Ortiz AL, Shaw L (2004) X-ray diffraction analysis of a severely plastically deformed aluminium alloy. Acta Mater 52:2185–2197. https://doi.org/10.1016/j.actamat.2004.01.012
60. Ilican S, CaglarY CaglarM (2008) Properties of ZnO thin films prepared by reactive evaporation. J Optoelectron Adv Mater 10:2578–2583
61. Favero PP, de Soza-parise M, Fernandez JLR, Mitto R, Ferraz AC (2006) Surface properties of CdS nanoparticles. Braz J Phys 36:1032–1034
62. Siow KS, Bitcher L, Kumar S, Griesser HJ (2006) Plasma methods for the generation of chemically reactive surfaces for biomolecule immobilization and cell colonization—a review. Plasama Process Polym 3:392–418. https://doi.org/10.1002/ppap.200600021
63. Vorokh AS, Rempel AA (2007) Atomic structure of cadmium sulfide nanoparticles. J Phys Solid State 49:143–148
64. Yesu Thangam Y, Anitha R, Kavitha B (2012) Novel method to synthesize and characterize zinc sulfide nanoparticles. Int J Appl Sci Eng Res 1:282–286. https://doi.org/10.6088/ijaser.00201001029
65. Vengala Rao B, Bhaskar Kumar G, Jayasimhadri M, Kiwan J, Ho-Sureb L, Yi Soung-Soo, Jeong JH (2011) Photoluminescence and structural properties of $Ca_3Y(VO_4)3:RE^{3+}$ (¼$Sm^{3+,}$ Ho^{3+} and Tm^{3+}) powder phosphors for tri-colors. J Cryst Growth 326:120–123. https://doi.org/10.1016/j.jcrysgro.2011.01.075
66. Thirumala Rao G, Babu B, Joyce Stella R, PushpaManjaribV VenkataReddy, Ch JaesoolShim, Ravikumar RVSSN (2015) Synthesis and characterization of VO^{2+} doped ZnO–CdS composite nanopowder. J Mol Struct 1081:254–259. https://doi.org/10.1016/j.molstruc.2014.10.044
67. Nakamoto K (1997) Infrared and Raman spectra of inorganic and coordination compounds, part-A, 5th edn. Wiley, New York
68. Pushpa Manjari V, Rama Krishna Ch, Venkata Reddy Ch, Ravikumar RVSSN (2014) Synthesis and spectral investigations of Cu(II) ion-doped $NaCaAlPO_4F_3$ phosphor. J Lumin 29:1123–1129
69. Mahmoud WE (2017) Synthesis and characterization of 2A-3SHPA decorated ZnS@CdS core–shell hetrostructure nanowires as a fluorescence probe for antimony ions detection. Sens Actuators B 238:1001–1007. https://doi.org/10.1016/j.snb.2016.07.150
70. Sperling RA, Park WJ (2010) Surface modification fictionalization and bio conjugation of colloidal inorganic nanoparticles. Philos Trans R Soc A 368:1333–1383. https://doi.org/10.1098/rsta.2009.0273